Comparative modelling of the coupled thermal–hydraulic-mechanical (THM) processes in a heated bentonite pellet column with hydration

B. J. Graupner[1] · H. Shao[2] · X. R. Wang[2] · T. S. Nguyen[3] · Z. Li[3] · J. Rutqvist[4] · F. Chen[4] · J. Birkholzer[4] · W. Wang[5] · O. Kolditz[5] · P. Z. Pan[6] · X. T. Feng[6] · C. Lee[7] · K. Maekawa[8] · S. Stothof[9] · C. Manepally[9] · B. Dasgupta[9] · G. Ofoegbu[9] · R. Fedors[10] · J. D. Barnichon[11] · E. Ballarini[12] · S. Bauer[12] · B. Garitte[13]

[1] Swiss Federal Nuclear Safety Inspectorate (ENSI), Brugg, Switzerland [2] Federal Institute for Geosciences and Natural Resources (BGR), Hanover, Germany [3] Canadian Nuclear Safety Commission (CNSC), Ottawa, Canada [4] Lawrence Berkeley National Laboratory (LBNL), Berkeley, USA [5] Helmholtz Centre for Environmental Research (UFZ), Leipzig, Germany [6] State Key Laboratory of Geomechanics and Geotechnical Engineering, Institute of Rock and Soil Mechanics, Chinese Academy of Sciences (CAS), Wuhan, China [7] Korea Atomic Energy Research Institute (KAERI), Daejeon, South Korea [8] Japan Atomic Energy Agency (JAEA), Tokyo, Japan [9] Center for Nuclear Waste Regulatory Analyses (CNWRA), Rockville, USA [10] Nuclear Regulatory Commission (NRC), Rockville, USA [11] Institute for Radiological Protection and Nuclear Safety (IRSN), Paris, France [12] Institute of Geosciences, University of Kiel, Kiel, Germany [13] National Cooperative for the Disposal of Radioactive Waste (NAGRA), Wettingen, Switzerland

Abstract

For the deep geological disposal of high-level radioactive waste in argillaceous rocks, the heat production of the waste is an important driver for thermal–hydraulic-mechanical (THM)-coupled processes. These THM processes influence the properties and conditions of the near field that in many repository designs contains bentonite as a clay buffer. One task in the DECOVALEX-2015 (DEvelopment of COupled models and their VALidation against Experiments) project was the modelling of a heated bentonite column (Villar et al. in Long-term THM tests reports: THM cells for the HE-E test: update of results until February 2014. Deliverable-no: D2.2-7.3. CIEMAT Technical Report IEMAT/DMA/2G210/03/2014, 2014) in preparation for the in situ heater experiment HE-E at the underground rock laboratory Mont Terri. DECOVALEX is an international cooperative project that focuses on the development and validation of mathematical models for simulating such coupled processes associated with disposal in deep geological repositories. Eight modelling teams developed their own THM-coupled models for the bentonite column experiment, using six different simulation codes. Each of the teams individually calibrated the THM parameters for the bentonite material. The eight resulting parameter sets agree well and allow a satisfactory reproduction of the TH measurements by all models. The modelling results for the evolution of temperature and relative humidity over time at three sensors in the bentonite column are in good agreement

between the teams and with the measured data. Also, changes of the temperature due to modifications of the insulation and the adjustment of the heating power during the course of the experiment are well reproduced. The models were thus able to reproduce the main physical processes of the experiment, both for vapour-dominated diffusion during the heating phase and combined liquid and vapour transport during a subsequent heating and hydration phase. Based on the parameter sets, the teams predict a penetration of the water infiltration front in the 48-cm column filled with bentonite pellets to a depth between 25 and 35 cm over the 15,000 h (i.e. over 20 months) of the hydration phase of the experiment.

Keywords

Mont Terri, Clay rock, Bentonite, Heater experiment, Coupled THM processes

Introduction

Deep geological disposal is currently considered as the most feasible solution for the long-term disposal of high-level radioactive waste (HLW). Due to the continuous decay of radionuclides, HLW produces heat, thus the repository will impose thermal impact upon the surrounding argillaceous, granitic or salt host rocks. Argillaceous rocks have a lower heat conductivity than granite or salt, resulting in higher temperatures around the waste canister for a given heat load. The elevated temperature will directly increase the specific volume of water because of thermal expansion and may induce deformation of the rock, which in turn affects the pore water pressures due to poro-mechanical effects. A clay buffer is often proposed for repository designs hosted in argillaceous and granitic rocks.

The impact of heat production on buffer material and the surrounding rock was investigated with in situ experiments for several argillaceous rocks including the FE (Full-scale Emplacement) (Müller et al. 2012), the borehole-scale heater test HE-D (Wileveau 2005), and the mini-tunnel scale heater experiment HE-E (Gaus et al. 2014b) performed in the Opalinus Clay at the Mont Terri Rock Laboratory in Switzerland, and the full-scale heater test HA (Armand 2015) and the TER experiment (Wileveau and Su 2007) performed in the Callovo-Oxfordian (COX) Clay in the Meuse/Haute-Marne Underground Research Laboratory (URL) at the Bure site in France.

Within the PEBS project (www.pebs-eu.de), the 1:2 scale HE-E in situ heater experiment was carried out to improve the understanding of the thermal evolution of the near-field environment around a HLW canister during the early phase after emplacement (Gaus et al. 2014a, b). The HE-E experiment consists of two tunnel sections with heaters representing the waste canisters. One section is filled with pure MX-80 bentonite pellets (Wyoming sodium bentonite) and the other section with a mixture of 35% MX-80 and a 65% quartz that has higher thermal conductivities (Villar et al. 2014). Well-controlled laboratory thermal–hydraulic-mechanical (THM) experiments of the MX-80 and the sand/bentonite mixture (Villar et al. 2012, 2014) were

conducted to characterize the buffer materials, mimicking in the laboratory the expected field conditions of heating and hydration in the laboratory. The two column experiments were performed at the Centro de Investigaciones Energéticas, Medioambientales y Tecnológicas (CIEMAT) as a part of the PEBS project.

A comprehensive understanding of coupled THM processes will be a key element among others for the design of deep geological repositories. Experiments provide the necessary information on processes and their dependencies. The DECOVALEX project (www.decovalex.org), which started in the early 1990s, is an initiative that focuses on the development and validation of mathematical models for such coupled processes based on experiments. The project aims to understanding the long-term evolution and performance of multiple barrier systems considered in repository concepts and to validate the simulation capabilities for the relevant coupled THM and thermal–hydraulic-chemical (THC) processes in order to provide reliable prognosis of ongoing effects at such repositories. Reliability of long-term prognosis is obtained only through model inter-comparison, as no experiments can cover the timescales involved. Detailed model comparison and benchmarking is thus a way of strengthening trust in the models and the model predictions.

Task B1 was one out of five tasks in the 6th phase of DECOVALEX project (2012–2015). Task B1 considered a set of heating experiments, with the main objective of investigating the THM response to heating of argillaceous rocks and bentonite buffers. Task B1 included three subtasks:

Step 1a Modelling the HE-D experiment to study coupled THM processes in Opalinus Clay

Step 1b Modelling the CIEMAT column cells to study coupled THM processes in the buffer materials

Step 2 Modelling the HE-E experiment to study coupled THM processes in both the Opalinus Clay and the buffer materials

Step 1a used the HE-D heating experiment at the Mont Terri URL to examine the thermal responses of Opalinus Clay and to determine appropriate THM parameters for the rock mass. The results are documented in Garitte et al. (2016). Step 1b used data from a laboratory column experiment for MX80 bentonite pellets to examine the bentonite buffer material and its THM behaviour, and the results are documented in this paper. Step 2 examined the combined behaviour of Opalinus Clay and bentonite using the HE-E heating experiment at the Mont Terri URL. The relevant parameters identified in Steps 1a and 1b were used as a starting point in Step 2 analyses. The results are documented by Garitte et al. (2017).

Villar et al. (2012, 2014) document two laboratory column tests performed in parallel, considering the THM response of (1) MX80 bentonite pellets and (2) a sand/bentonite mixture. Each column test was intended to approximate the

buffer domain between the heater and host rock in the HE-E experiment for one of the buffer materials. Both column tests consisted of an initial thermal phase with two heater temperatures, followed by a hydration stage with the heater remaining on. This paper focuses on the column experiment for MX80 bentonite pellets. Results for the sand/bentonite mixture can be found in Wang et al. (2015) and Ballarini et al. (2017).

Eight modelling teams analysed the bentonite pellet column test. The column test posed a distinct numerical challenge, because the porous medium has a dual pore structure that may irreversibly alter during hydration. At the start of the test, each pellet consisted of dried bentonite at high suction and the pore space within each pellet (the micropores) was partially saturated. The initial pellet size distribution was similar to well-graded gravelly sand with silt, with an essentially dry macropore space between pellets. As all teams used a single continuum approach, the micro- and macro-porosity nature of the bentonite was not directly incorporated into the models. However, interpretation of results is aided by realizing this conceptualization of the dual-porosity nature of the bentonite pellet material. Conceptually, the initial macropores have a relatively large permeability, and the micropores have a very small permeability. As hydration proceeds, clay minerals swell, tactoids in adjacent pellets rearrange into a homogeneous clay mass, and total porosity decreases. Illustrating the interplay of geomechanical and hydrological processes, the number of micropores expands at the expense of the number of macropores during hydration. In the column test, micropore expansion dominates and axial pressure in the column increases. In this process, overall permeability, which is dominated by the macropore space, decreases (Seiphoori 2015). Subsequent drying would not recover the original state of the pellets.

This paper focuses on numerical simulation of the laboratory column experiment for MX-80 bentonite pellets. The paper describes (1) material properties for the relevant THM processes, (2) relevant processes considered with different models and modelling approaches, (3) a detailed comparison of the modelling results between the teams and with the measured data and (4) the sensitive parameters governing the simulations.

Description of the CIEMAT column experiment

Experimental set-up

The THM behaviour of MX-80 bentonite investigated in the column experiment intended to reproduce expected conditions in the later HE-E experiment (Villar et al. 2012, 2014). The HE-E experiment includes initial heating stages during which the buffer material is heated with minimal interaction between the buffer and host rock, followed by later stages when water from the host rock is anticipated to resaturate the buffer. Therefore, the column test experiment consisted of a heating phase followed by a heating and hydration phase.

The experimental set-up, described in detail by Villar et al. (2012, 2014), is shown in Fig. 1a. The column interior has a diameter of 0.07 m and a height of 0.4839 m. The bodies of the cells are made of Teflon to reduce heat conduction in the sample containment components. A layer of steel outside the column provided rigidity to avoid column deformation due to buffer swelling during the hydration phase. Additional layers of insulation were added during the course of the experiment (after 1518 h) to reduce the lateral heat loss. These changes are summarized in Table 1 and are graphically reported in Fig. 1b.

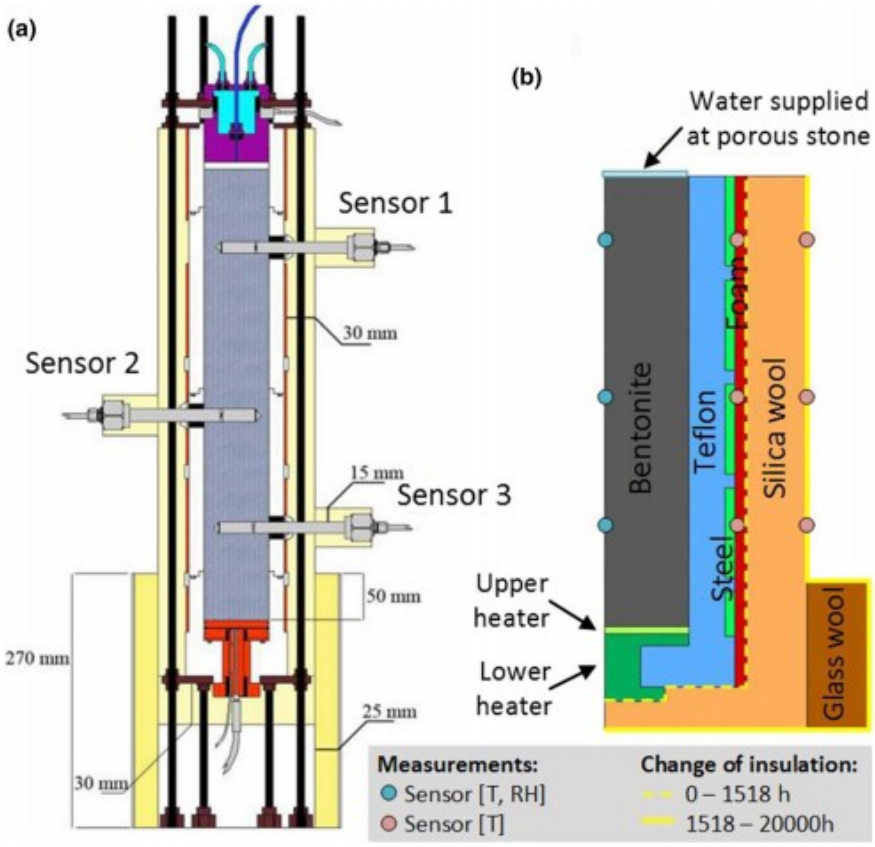

Fig. 1 **a** Full set-up for the experiment (Villar et al. 2012); **b** 2D axisymmetric representation (expanded two-fold in the horizontal direction) of the experimental set-up showing the different materials, the points of measurement (coloured dots), and the changes made to the insulation during the experiment

Table 1 Changes in the insulation and phases of the two experiments

Time from beginning of heating (h)	Insulation set-up	Phase
Exp–bentonite		
0–1518	0.015 m Teflon + 0.005 m insulation foam	Heating 100 °C
1518–3524	Teflon + 0.03 m insulation wool + 0.025 m Isover[#]	Heating 100 °C
3524–5012	Teflon + 0.03 m insulation wool + 0.025 m Isover	Heating 140 °C
5012–20,000	Teflon + 0.03 m insulation wool + 0.025 m Isover	Heating 140 °C + hydration

[#] Isover is a brand of insulation

In the experiments, the buffer material rested on a heater plate closing the bottom of the column. In the experiments, the buffer material rested on a

stainless-steel heater plate closing the bottom of the column. The power provided to the heater was dynamically adjusted to maintain the desired temperature on the upper heater plate.

The buffer material was capped by a porous stone at the top of the column. The porous stone was restrained by a steel plug penetrated by a hydration tube, and the plug was restrained in turn by a load cell and the upper plate. The load cell was used to measure the swelling pressure during the test. The plug was connected to a cooling system maintained at the laboratory temperature. The hydration tube provided the only means of mass exchange during the experiment and was closed during the heating phase. During the hydration phase, the hydration tube connected the porous stone with a sodium-rich Pearson water solution (Pearson et al. 2003) at laboratory temperature in an elevated source water bottle. The source water bottle was not pressurized and had an initial overpressure of about 0.1 bar due to the elastic behaviour of the bottle. Water intake was measured by the changing weight of the source water bottle.

The initial saturation of the MX-80 bentonite was 22% throughout the column. The heating phase imposed a step temperature increase at the heater plate from ambient temperature to 100 °C, followed by a later step (from 100 to 140 °C). The heating phase lasted for 5012 h, and the hydration phase continued until the end of the experiment after about 20,000 h.

Properties of the MX-80 bentonite pellets

The column was filled with a compacted MX-80 bentonite granulate (bentonite pellets) without additional compaction. The pellets have a dry solid particle density of 2.75 g cm^{-3}. After emplacement in the column, the dry bulk density of the filling material was 1.53 g cm^{-3}, with an initial water content of 6.4% by weight (Villar et al. 2014). The THM properties of MX-80 bentonite are investigated in several studies. Wieczorek et al. (2011, 2013), Villar (2005) and Rizzi et al. (2012) investigated the dependency of the thermal parameters and water retention curve on temperature and degree of saturation, indicating that the temperature influence on the thermal parameters is not very significant compared to changes in water content. Tang and Cui (2006, 2010) found proportionality among thermal conductivity, dry density and water content. Additionally, the mineralogical effect is significant on the thermal conductivity and swelling capacity. Wang et al. (2012) studied the swelling behaviour of the MX-80, concluding that upon wetting, the swelling pressure increases with decreasing suction. Rizzi et al. (2012) indicated that at high temperature, the montmorillonite mineral may change to a more stable silicate phases without the possibility of retaining interlayer water, thus losing its swelling capacity. However, the temperatures reached in the CIEMAT column experiments do not likely reach those needed for dewatering of the minerals or other mineral alterations.

Measurements

The cell was instrumented with three sensors measuring temperature and relative humidity (Sensors 1, 2 and 3) placed inside the bentonite material at 40, 22 and 10 cm from the heater plate (see Fig. 1a, b). Additional measurements include temperature on the top of the heater plate and inside the insulation, but Villar et al. (2014) only provide an average value for the last 9 months of the experiments for the latter.

The power supplied to the heater was measured during the experiments and was dynamically adjusted to maintain the desired temperature on the top of the heater plate (Fig. 2a); applied power fluctuated by ~ 2 W over the course of a day (Villar et al. 2012). The heating phase consisted of three stages (Table 1). The first two stages held the heater at 100 °C, and the third held the heater at 140 °C. Improved insulation installed after 1518 h reduced the power necessary to maintain a temperature of 100 °C from 12.5 to 8 W while increasing temperature throughout the column. In the third stage (5012 h), a heater temperature of 140 °C required an average heater power of 12 W.

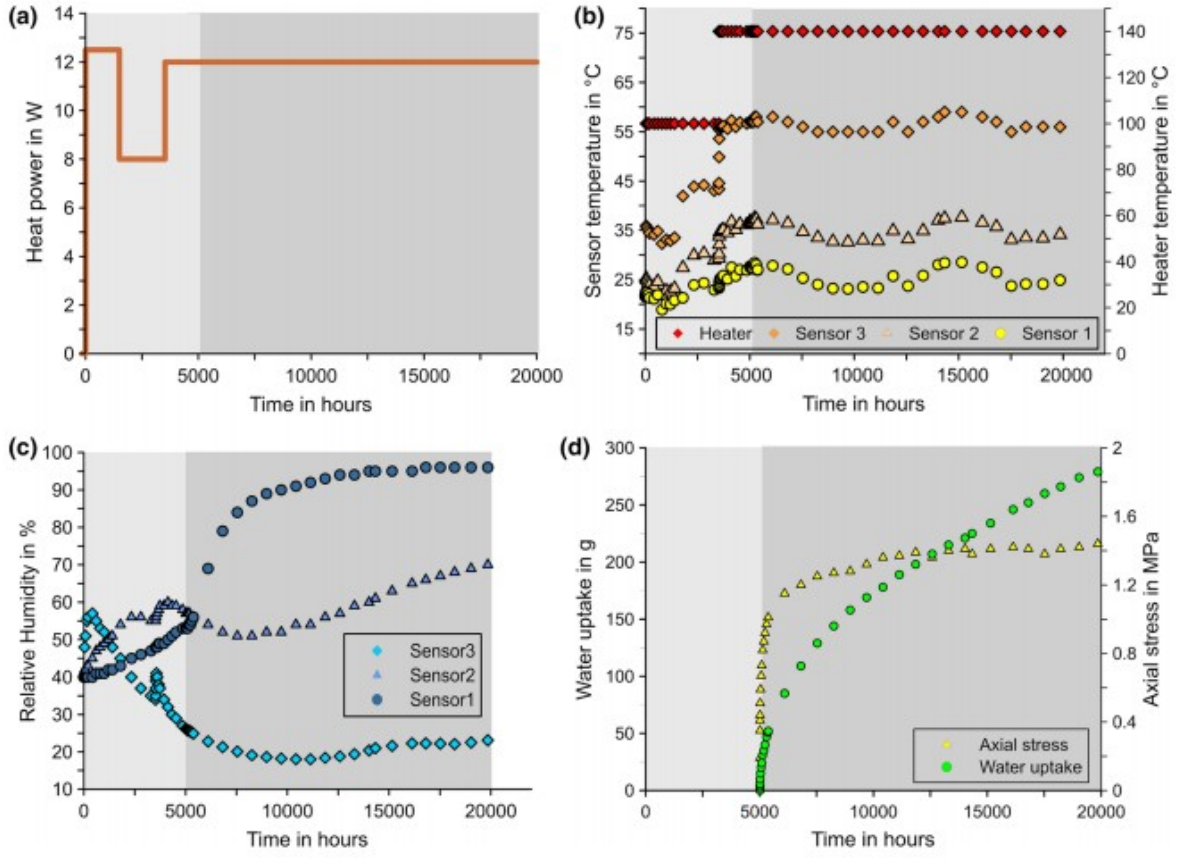

Fig. 2 Measurements for **a** applied heat power; **b** temperature evolution at the three sensors (left axis) and at the heater (right axis); **c** relative humidity evolution at the three sensors; **d** water intake (left axis) and axial load (right axis). The heating (light grey area) and the hydration phase (dark grey area) are shaded on each plot. (Data from Villar et al. 2014)

Temperature evolution at the sensors in the bentonite column reflects the effect of variations in the ambient laboratory temperature, heat advection by

liquid water and water vapour, and altered thermal conductivity due to the changes in the saturation of the buffer materials. Temperatures equilibrated at all sensors within 1–3 days after a change in heat load. A temperature change with similar magnitude simultaneously observed in all sensors is due to a change in laboratory temperature (especially evident after 4000 h in Fig. 2b), which varied by at least 5 °C over the experimental period. Effects of laboratory air temperature fluctuations overlay on any effects of heat advection and altered thermal conductivity. The movement of water vapour caused by the thermal gradient is indicated by the strong increase of relative humidity at Sensor 3 and Sensor 2 at the beginning of the heating phase and the long-term decrease in relative humidity at Sensor 3 balanced by an increase at Sensors 1 and 2 (Fig. 2c).

The axial pressure generated during the hydration phase as recorded at the load cell positioned at the top of the column is shown in Fig. 2d. The axial pressure increased during the hydration phase due to the swelling of the bentonite. Small fluctuations in axial pressure may be linked to changes in laboratory temperature. The internal change in air pressure is an order of magnitude too small to explain these fluctuations.

Villar et al. (2014) documented the average temperature gradient through the experimental set-up of the bentonite column (Fig. 3). The sensors indicate that the heat flux is from the bentonite into the steel shell nearest the heater and is reversed in the middle of the column. The uppermost sensors are located at a gap in the steel shells and show smaller heat fluxes. The steel shells are much more thermally conductive than the bentonite and Teflon, strongly influencing the heat flux patterns.

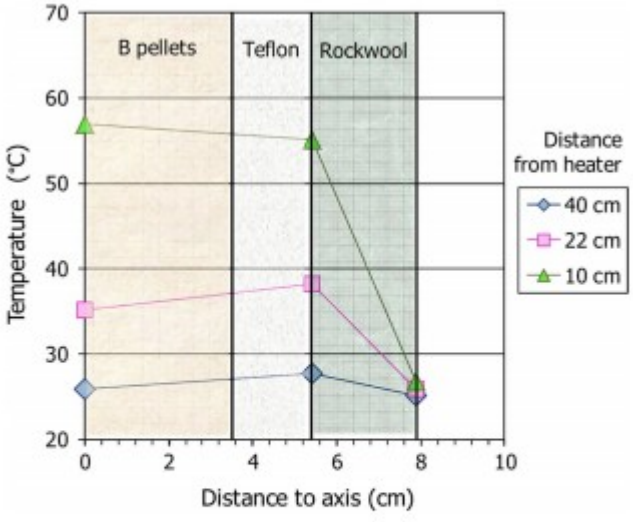

Fig. 3 Average temperature at the three sensor heights (legend, vertical distance from heater) for different radial distances (0…centre of the bentonite column) from June 2013 to February 2014 (≈ 8600 h) from Villar et al. (2014). The average laboratory temperature during this period was 20.9 ± 1.2 °C

Modelling approaches

Conceptualization, teams and modelling approaches

The experiment was designed to have two heating phases (the heater held at 100 °C and then 140 °C) with the system closed to water and air, followed by a hydration phase with the heater held at 140 °C and water allowed to imbibe freely at the top of the column. The experiment followed this plan, except that excessive heat loss was addressed by wrapping the column in additional insulation midway through the first heating phase.

During the heating phases, temperatures were expected to equilibrate rapidly into an approximately linear profile from the bottom (heater) to the top (cooled plug). The water remaining in the bentonite was expected to respond to changes in the thermal regime by evaporating near the heated bottom and condensing near the cooled top, dominated by vapour transport and with minimal liquid transport in the dry pellets. The rate of vapour transport was expected to decrease to zero as the vapour density equilibrated throughout the column. The redistribution of water was expected to decrease the thermal conductivity in the dryout zone and increase it in the condensation zone. The addition of condensing water at the top of the column was expected to cause the bentonite to swell. At the bottom of the column, it was not clear whether the bentonite response would be primarily expansion from heating or shrinking from drying.

It was less clear exactly how the water would hydrate the bentonite, because of the dual-porosity nature of the bentonite pellets. The overall texture of the medium formed by dry pellets is like well-graded gravelly sand, which would be expected to imbibe rapidly because of high suction. However, entry of water was expected to trigger the swelling process, rapidly dropping the effective permeability from a sand-like value to a clay-like value in the wetted bentonite. Once swelling transformed the pellets into a thin layer of low-permeability clay next to the porous stone, water was expected to imbibe at a rate consistent with diffusive imbibition into clay with countercurrent displacement of the nonwetting air phase. For two incompressible phases, the inflow flux is proportional to $t^{-1/2}$ in the exact analytical solution (McWhorter and Sunada 1990), so long-term cumulative imbibition was expected to scale approximately as $t^{1/2}$. Quasi-equilibrium adjustment to the thermal conductivity and relative humidity profile was expected to occur as the wetting front slowly progressed. The wetted bentonite was expected to increase the pressure on the load cell at a rate roughly proportional to the rate of water imbibition.

Eight research teams involved in DECOVALEX Task B1 simulated the column test. Table 2 shows the colour code associated with each team, which will be used later in this paper for the comparison of modelling results. Table 2 also indicates the computer codes, the associated numerical methods, the considered coupled processes and the model dimension used by the teams.

Table 2 Colour codes, computer codes, numerical methods, considered processes, model dimension, and representation of the source term and lateral boundary in the model used by the teams in Task B1

Team & Colour Code	Code	Numerical method	Hydrological approach	Model dimension	Heat source term	Lateral boundary
BGR/UFZ	OpenGeoSys	FEM	2-phase flow	2D axisymmetric	Heat power	Temperature & heat loss coefficient
CAS	EPCA3D	EPCA	2-phase flow	3D	Temperature	Temperature
LBNL/DOE	TOUGH-FLAC	IFD/FDM	2-phase flow	2D axisymmetric	Temperature	Temperature
ENSI/CAU	OpenGeoSys	FEM	2-phase flow	2D axisymmetric	Heat power	Temperature
CNSC/IRSN	COMSOL	FEM	1-phase flow	2D axisymmetric	Temperature	Heat loss coefficient
JAEA	THAMES	FEM	1-phase flow	3D	Temperature	Heat loss coefficient
KAERI	TOUGH-FLAC	IFD/FDM	2-phase flow	3D	Heat power	Temperature
CNWRA/NRC	xFlo-FLAC	IFD/FDM	2-phase flow	2D axisymmetric	Temperature	Temperature

UFZ: Helmholtz Centre for Environmental Research; BGR: Federal Institute for Geosciences and Natural Resources; CAS: State Key Laboratory of Geomechanics and Geotechnical Engineering, Institute of Rock and Soil Mechanics, Chinese Academy of Sciences; LBNL: Lawrence Berkeley National Laboratory; DOE: U.S. Department of Energy; ENSI: Swiss Federal Nuclear Safety Inspectorate; CAU: Institute of Geosciences, University of Kiel, Germany; CNSC: Canadian Nuclear Safety Commission; IRSN: French Institute for Radiological Protection and Nuclear Safety; JAEA: Japan Atomic Energy Agency; KAERI: Korea Atomic Energy Research Institute; CNWRA: SwRI Center for Nuclear Waste Regulatory Analyses; NRC: U.S. Nuclear Regulatory Commission; FEM: Finite Element Method; IFD: Integral Finite Difference Method; FDM: Finite Difference Method; EPCA: Elasto-Plastic Cellular Automaton Method

The computer codes used are based on different numerical methods. Teams BGR/UFZ and ENSI/CAU used the finite element method, with the object-oriented OpenGeoSys computer code (Kolditz et al. 2012; Kolditz and Bauer 2004) and specific enhancements for non-isothermal flow described in Wang et al. (2015). Teams CNSC and JAEA also used the finite element method, with the COMSOL (Nguyen et al. 2016) and THAMES codes (Ohnishi et al. 1985), respectively. CAS team used a self-developed numerical code EPCA^{3D}, which is a combination of multiple techniques and theories, such as finite element method, cellular automaton, elasto-plastic theory and principle of statistics (Pan et al. 2009a, b; Pan and Feng 2013). The CNWRA/NRC team linked the Integral Finite Difference multiphase code xFlo (Stothoff and Painter 2016) to the Finite Difference code FLAC (Itasca Consulting Group 2011). KAERI team and the LBNL team used TOUGH-FLAC, based on linking the TOUGH2 multiphase flow simulator (Integral Finite Difference), with the FLAC3D geomechanical code (Itasca 2012, Finite Difference Method) (Rutqvist et al. 2002, 2014).

Models and parameterization

The teams considered different model domains in order to represent the two different insulation configurations for the bentonite column experiment. Examples of model grids used to represent the final insulation configuration, including the different materials, are shown in Fig. 4. Some of the teams used a detailed representation of the experimental set-up, including the heater and base as part of the model, whereas others represent the heater as a boundary condition to the bentonite column with a simplified geometry of the experimental set-up.

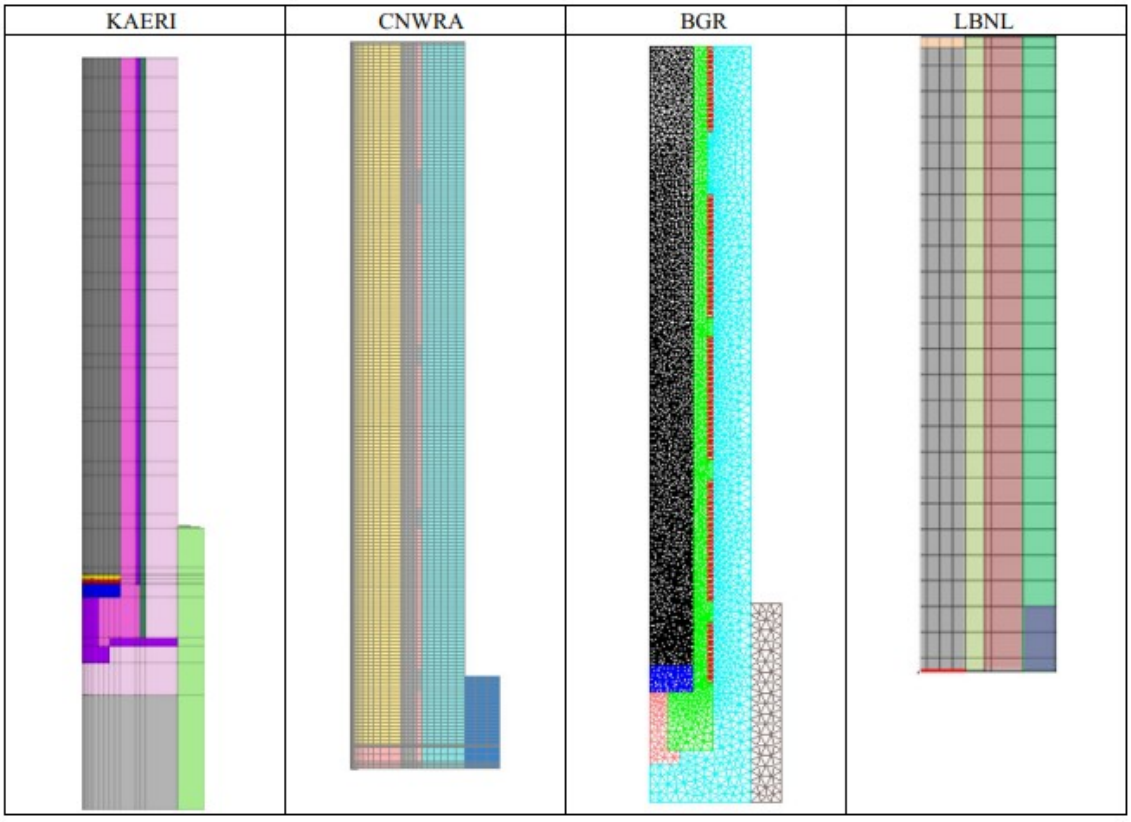

Fig. 4 Examples of model geometries used by the teams. All examples utilize radial symmetry, but may incorporate different sets or representations of components or extents of modelling domain

The model set-up constrained how some teams applied thermal boundary conditions, because models that considered a simplified geometry could not directly calculate the substantial heat losses below the heater and therefore had difficulties in imposing a heat source condition at the heater. The simplified models used a specified temperature boundary condition instead of a heat source condition. Calibrating bentonite thermal properties requires that heat fluxes to the bentonite are accurately estimated, thus teams directly applying the heater temperature as a boundary condition needed additional steps to verify that the fraction of the heat flux applied to the bentonite was appropriate. For example, the CNWRA/NRC team constructed a third model in COMSOL, considering just thermal processes with a highly detailed geometric representation, to develop confidence in thermal conductivity values, compare temperature and power for the heater boundary conditions and support simplification of the xFlo-FLAC grid (Stothoff et al. 2015).

All teams initially treated the bentonite pellets as a single continuum rather than explicitly addressing the dual continuum nature of the medium. The main parameters used for the characterization of the THM properties of bentonite are shown in Table 3. The heat conductivity, the capillary saturation function and the relative permeability depend on the water

saturation. Thus, the relationships used by the teams are shown in Figs. 5, 6 and 7.

Table 3 Main bentonite parameters considered by the teams; $F(T)$ and $F(s)$ denote functions of temperature and suction respectively

		BGR/UFZ	CAS	LBNL	ENSI/CAU	CNSC	JAEA	KAERI	CNWRA
Porosity (–)	φ	0.44	0.444	0.44	0.444	0.45	0.444	0.444	0.444
Tortuosity (–)	τ	0.67	1.0	0.67	0.8	0.5	1.0	0.8	–
Intrinsic permeability (m^2)	k	4.5e−21	9.5e−20	5.5e−21	2.0e−20	1.0e−21	3.0e−20	5.0e−21	7.7e−21
Solid particle density (kg m^{-3})	ρ_s	2732	2750	2750	2750	2750	2750	2750	2750
Bulk density (kg m^{-3})	ρ_b	1530	1530	1540	1530	1513	1530	1530	1530
Dry thermal conductivity (W $m^{-1}K^{-1}$)	λ	0.3	0.3	0.28	0.3	0.35	0.17	0.4	0.325
Wet thermal conductivity (W $m^{-1}K^{-1}$)	λ_S	1.0	1.1	1.2	1.04	1.3	0.83	1.0	1.114
Thermal expansion (K^{-1})	b_s	1.0e−5	1.0e−5	1.0e−5	1.0e−5	2.5e−5	1.0e−6	2.6e−6	1.0e−5
Heat capacity (J $kg^{-1}K^{-1}$)	C	950	950	950	$F(T)$	800–1500	500	960	640
Poisson's ratio (–)	ν	0.35	0.35	0.35	0.35	0.35	0.3	0.35	0.3
Young's modulus (MPa)	E_h	18	18	18	18	18	34	40.0	–
Bulk modulus (MPa)							–		21–48, $F(s)$
Maximum swelling pressure (MPa)	p_{sw}	7.3	4	4	4		4.3	3.0	–
Biot coefficient (–)	b	1.0	0.7	1.0	1.0		–	0.6	–
Bishop coefficient (–)		–	1.0		$F(s)$		–		$F(s)$

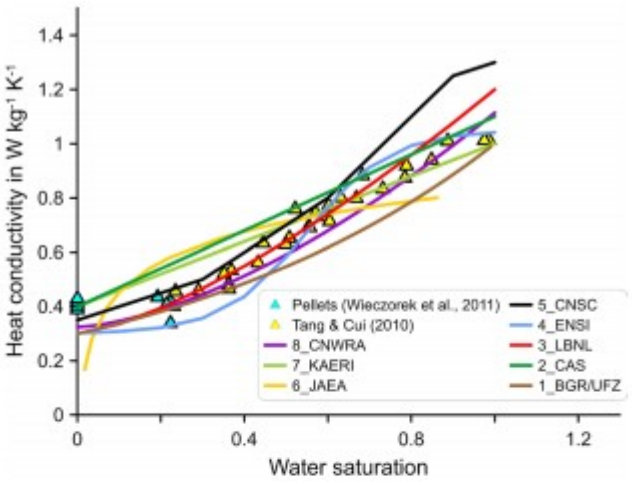

Fig. 5 Thermal conductivity values as function of the water saturation used by the teams and measured data by Wieczorek et al. (2011) and Tang and Cui (2010)

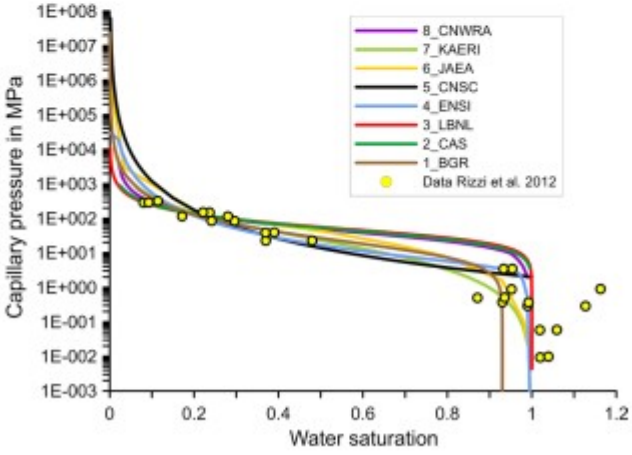

Fig. 6 Capillary pressure–water saturation function used by the teams and measured data from Rizzi et al. (2012)

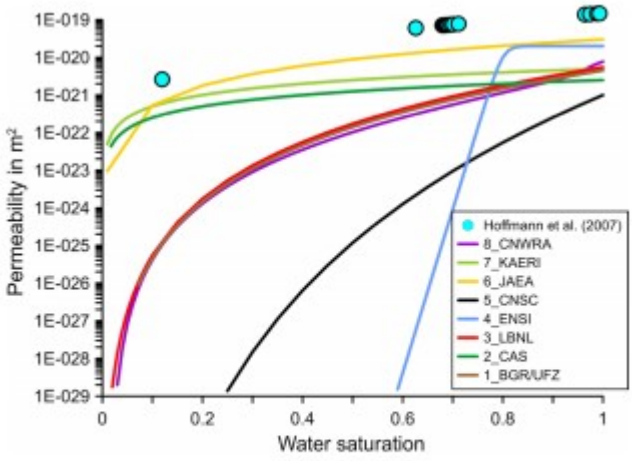

Fig. 7 Permeability–water saturation function used by the teams and measured data by Hoffmann et al. (2007)

Each team individually evaluated the relationship between the bentonite thermal conductivity and its water saturation, using available measurements from Wieczorek et al. (2011) and Tang and Cui (2010) or others. Each team considered the measured temperatures in the bentonite column, the measured heater temperature and the uncertain heat loss through the lateral and bottom boundaries in evaluating the relationship. Figure 5 shows the relations used by the teams. Most of them have a thermal conductivity of 0.3–0.4 W $m^{-1}K^{-1}$ at low water saturation and a thermal conductivity of 1–1.2 W $m^{-1}K^{-1}$ at high water saturation.

The relationship between capillary pressure and water saturation was fitted based on measurements from Rizzi et al. (2012), the initial water content of bentonite and the relative humidity measured in bentonite at the beginning of the experiment. Some teams additionally considered temperature-dependent retention curves. Each team selected their own values for the intrinsic permeability and the functional relationship between relative permeability and water saturation. These were adjusted based on few available data from Hoffmann et al. (2007) and on the saturation behaviour of bentonite during the hydration phase.

During calibration, teams that used a two-phase flow formulation (i.e. explicitly modelling advective gas movement) had difficulty representing the gas dynamics and vapour transport, especially near the heater, using a single bentonite-based relationship for permeability. These models required that the high-permeability macropore space was also explicitly addressed for gas. The LBNL team developed a convenient heuristic approach for representing the large gas permeability in the macropore space, based on the mathematical model suggested by Klinkenberg (1941), and some teams adopted this approach. Gas and vapour transport was partly improved once the gas permeability was increased to 5 or 6 orders of magnitude larger than the water permeability under dry conditions. The teams recognize that this

heuristic approach has the form of the Klinkenberg model, but does not represent the physics of anomalous gas flow in very fine-textured media that the Klinkenberg model was developed to describe.

The teams were provided tabulated values of temperature, relative humidity, power input and axial pressure typically spaced at increasing intervals from hours to weeks. These values were only a small fraction of the data collected. The laboratory air temperature reported by Villar et al. (2012) fluctuated on diurnal, weekly and seasonal cycles, with the measured column temperatures apparently responding to daily to weekly fluctuations. Average applied power responded to changes in air temperature at approximately −0.35 to −0.4 W $°C^{-1}$ early in the hydration phase (Villar et al. 2014). Roughly consistent with isothermal oedometer measurements reported by Villar (2013) and the step changes in average column temperature due to changed insulation and increased heater temperature, it appears that the axial pressure also fluctuated slightly with the column temperature, perhaps 0.007–0.01 MPa $°C^{-1}$. All teams used the average applied power without correcting for power fluctuations. Some teams neglected the laboratory temperature fluctuations, some estimated fluctuating laboratory values for boundary conditions and some compared simulation results with de-trended values.

Modelling results and comparison with measurements from the column experiments

In this section, modelling results of the teams are indicated with the team colour and the measurements (if available) are indicated with symbols.

Figure 8 shows the measured and modelled temperature at the heater. Most of the teams applied the temperature as a boundary condition and the others used the heat power as a source term. The latter approach leads to slight deviations from the measured temperature, as obvious from Fig. 8. The figure contains only results from the three teams that applied heat power. One team used the average power input and average laboratory temperature for simulation boundary conditions. The other two teams estimated laboratory air temperatures to provide lateral boundary conditions, but used the average heat power (the actual applied power fluctuated with air temperature). The comparison with the measurements indicates that the reproduction of the heating system of the experiment is reasonable. There is a good agreement between the modelled and measured temperature during the first 3500 h of the heating phase despite the modification of the insulation after 1500 h. With the increasing temperature to 140 °C, deviations increase. Some teams calculated the heat flux going into the bentonite, finding that only 10–20% of the power applied to the heating device of the experiment was transferred directly into the bentonite as heat flux. Up to 65% of the applied power bypassed the bentonite, passing up the column in the Teflon column walls and (especially) in the steel bands, with most of this heat flux dissipating to the environment

through the insulation. The remainder of the heat flux was dissipated to the environment from the apparatus below the heater. Detailed numerical modelling by the NRC-CNWRA team illustrated the importance of experimental components, such as the steel supporting bands, for the heat transfer.

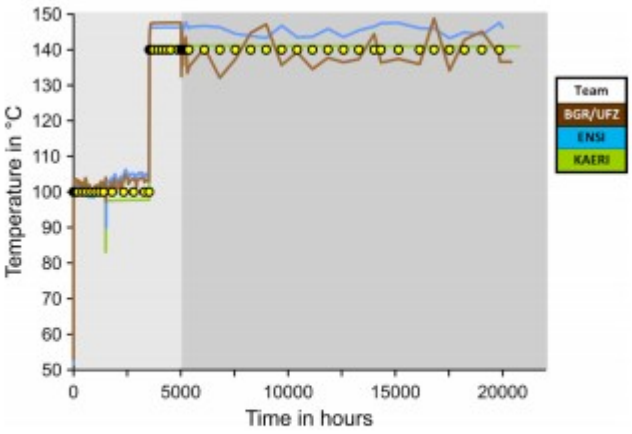

Fig. 8 Comparison of the modelled temperatures at the heater with the measurements (circle) during the heating (light grey area) and the hydration phase (dark grey area)

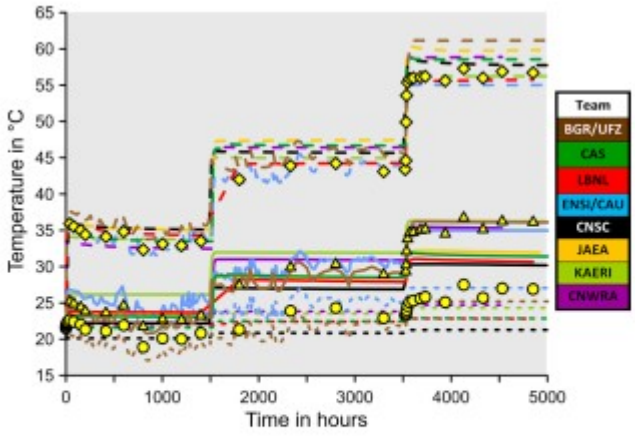

Fig. 9 Measured and modelled temperature at Sensor 1 (circles and dotted lines), at Sensor 2 (triangles and full lines) and at Sensor 3 (diamonds and dashed lines) during the heating phase (light grey area)

The measured and calculated evolution of the temperature within the bentonite column at Sensors 1 to 3 is shown in Fig. 9 for the first 5000 h (heating phase) and in Fig. 10 for up to 20,000 h (heating and hydration phase). The temperature of 100 °C is reached approximately 10 h after starting the heating phase. Modelling results are in good agreement between the teams and with the measured data. The modelling results adequately reflect the sharp temperature increase due to the improvement of the insulation after 1500 h and due to the increased heat power after 3500 h.

The variation of the measured temperatures after the first few days of a step change closely track changes of the average daily laboratory temperature, which varied between ~ 16 and ~ 22 °C during the entire experiment. Teams with fluctuating temperatures used the measured laboratory temperature over time as a boundary condition instead of an average value. The spread between the modelling results increases with increasing distance of the sensor from the heater, which is likely caused by different modelling choices for calculating (1) heat losses and (2) heat fluxes in the steel and Teflon walls. Some teams chose to impose a temperature boundary condition on the cell wall, with different selected temperatures; others used a heat loss condition. The measurements in Fig. 3 suggest that heat exchange occurred between the bentonite and steel, and teams selecting a constant heat loss for the boundary condition may have missed this influence.

The measured and modelled temperature profiles from the centre of the bentonite cell towards the outer boundary of the insulation are shown in Fig. 11. The data representing the boundary between Teflon and insulation were obtained from the steel shell encasing the Teflon. Model calculations suggest that each shell has a nearly uniform temperature because of its very large thermal conductivity relative to bentonite and Teflon. Therefore, the models calculate heat fluxes from the bentonite into the steel shell in the bottom half of each shell and heat fluxes from the steel shell into the bentonite in the top half of each shell. The bentonite temperature at the centre of the column can be several degrees warmer or cooler than the adjacent steel shell at the top and bottom of each shell. The sensor locations correspond to the middle of the steel shells for the two hottest profiles and intermediate between shells for the coolest profile, so the models suggest that lateral temperature gradients are relatively small. The measured data indicate temperature gradients comparable to model predictions, even though the gradients are displaced relative to the model calculations.

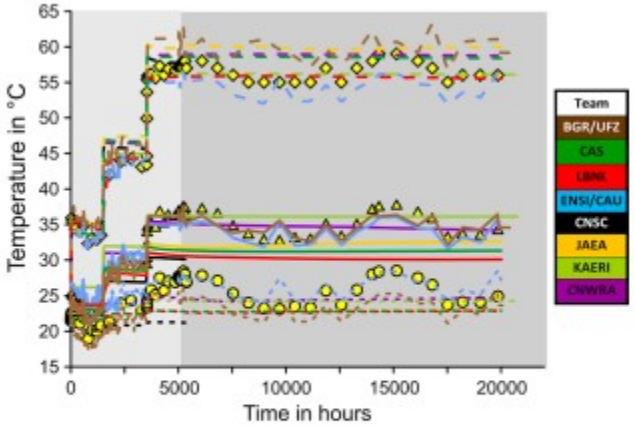

Fig. 10 Measured and modelled temperature at Sensor 1 (circles and dotted lines), at Sensor 2 (triangles and full lines) and at Sensor 3 (diamonds and dashed lines) during the heating (light grey area) and the hydration phase (dark grey area)

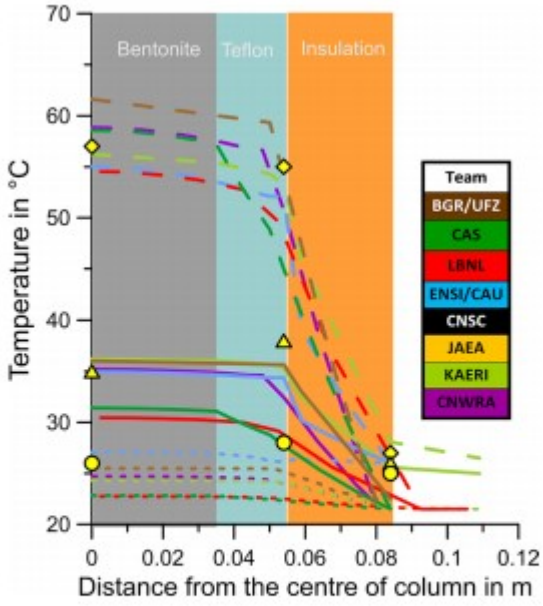

Fig. 11 Horizontal measured average temperatures and modelled temperature profiles after 5000 h from the centre of the bentonite cell towards the outer boundary of the insulation at the height of Sensor 1 (circles and dotted lines), of Sensor 2 (triangles and full lines) and of Sensor 3 (diamonds and dashed lines)

Figure 12 compares measured and modelled vertical profiles for the temperature and the relative humidity as well as the modelled water saturation within the bentonite. The initial expectation of approximately linearly varying temperature is not followed because of the heat lost from the cell surface. Some of the temperature, relative humidity and saturation profiles show slight oscillations corresponding to local temperature effects

near gaps between the steel shells. The temperature profile shows a good agreement between all teams. Temperature profiles are influenced by the thermal conductivity of the bentonite and thus by its degree of saturation. The modelled vertical profiles of water saturation after 5000 h (Fig. 12c) show that the initial water saturation at 22–25% has evolved to values between 1 and 30% during the heating phase as a consequence of water redistribution. In this range of water saturation, the heat conductivity of bentonite varies between ~ 0.2 and ~ 0.5 W $m^{-1}K^{-1}$. The good reproduction of the temperature profile provides some evidence that the models correctly reproduce the coupled effects of water redistribution during heating and the saturation dependence of the bentonite thermal conductivity. However, it should be recognized that the temperature profiles may be predominantly affected by the representation of the steel shells.

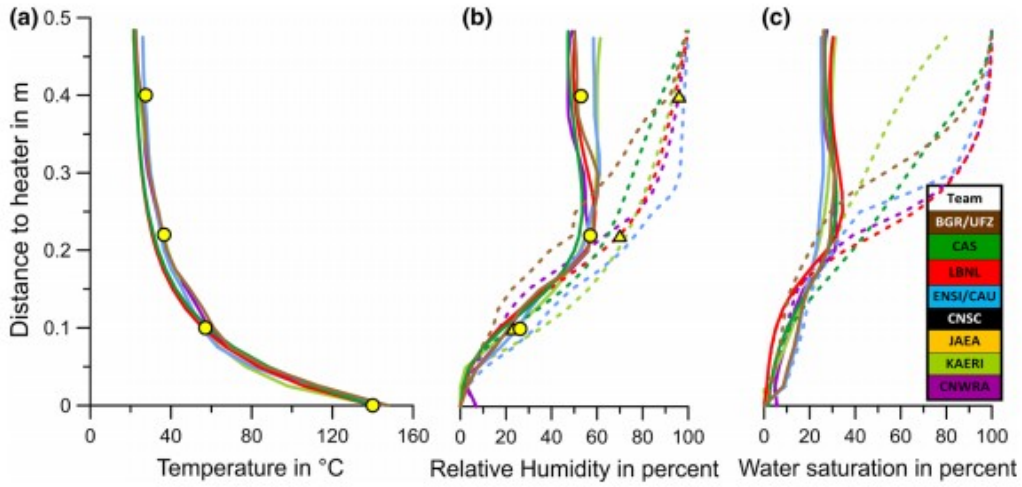

Fig. 12 Vertical measured and modelled profiles in the bentonite **a** for the temperature after 5000 h (circles and full lines) and **b** for the relative humidity after 5000 h (circles and full lines) and after 20,000 h (triangles and dotted lines and **c** the modelled water saturation after 5000 h (full lines) and after 20,000 h (dotted lines)

Measured and modelled relative humidity at the three sensors in the bentonite is compared for the heating phase in Fig. 13. The relative humidity traces show distinct patterns after changes in thermal regime. Sensor 3 shows a distinct peak in relative humidity ~ 400 h after start of heating and ~ 40 h after the heater temperature was increased to 140 °C. Sensor 2 shows the same pattern over a longer timescale, and Sensor 1 shows indications of a similar pattern over even longer timescales. The consistent pattern of rising relative humidity followed by a decline is symptomatic of evaporation from a heated drying front, with vapour transport down the temperature gradient and condensation in cooler zones. The peak occurs as the drying front begins to reach the sensor location. Following the increase in insulation, all three sensors also show a rapid jump in relative humidity of ~ 1–2.5% with a simultaneous temperature increase of 2–10 K (Villar et al. 2012, Figure 30), suggesting that the direct effect of temperature change on relative humidity is smaller than the effect of moisture redistribution.

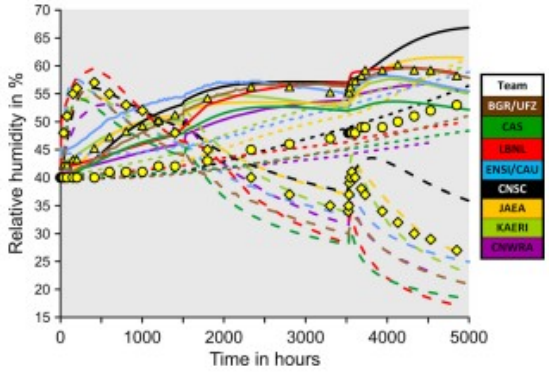

Fig. 13 Measured and modelled relative humidity at Sensor 1 (circles and dotted lines), at Sensor 2 (triangles and full lines) and at Sensor 3 (diamonds and dashed lines) during the heating phase (light grey area)

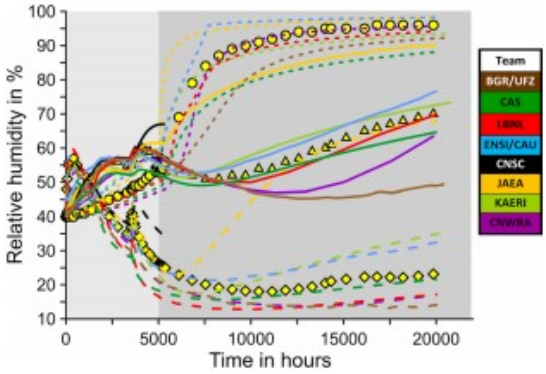

Fig. 14 Measured and modelled relative humidity at Sensor 1 (circles and dotted lines), at Sensor 2 (triangles and full lines) and at Sensor 3 (diamonds and dashed lines) during the heating (light grey area) and the hydration phase (dark grey area)

The modelling results of the teams reproduce in general all these changes of the relative humidity over time at the different sensors. Some of the models closely agree with the measurements, but the spread between the modelling results increases with time and reaches total values of 20% and more. One reason for the higher differences may be the less well-defined end points of the capillary pressure–water saturation relationship. The teams calibrated their individual relationships based on the available measurements (Fig. 6), and they agree well within a range of water saturation of 20–40%. With the drying or wetting process, the saturation changes and thus the differences of the resulting capillary pressure increase between the teams. This underlines the sensitivity of relative humidity calculations from the capillary pressure–water saturation relationship. Additional experimental investigations may help to limit the range of possible capillary pressure–water saturation relationships.

Measured and modelled relative humidity (RH) at the three sensors is compared for the entire experiment, covering both the heating and hydration phases, in Fig. 14. The rate of increase for measured RH at Sensor 1 inflected upwards within 250 h after the start of hydration, reaching values above 90% within 4700 h. RH continued to decrease at Sensors 2 and 3 for another 3300 and 5800 h after start of hydration, respectively, before beginning to increase (Villar et al. 2014). These patterns of increasing RH suggest that the wetting front from the hydration progressively overcomes the thermally induced vapour diffusion with some combination of downward liquid movement and saturation-induced vapour redistribution. The modelling results of the teams reproduce the increasing RH, the general shape of the curves and the time lag between the sensors quite well. The spread between the calculated total values might again be caused by the variation between the capillary pressure–water saturation relationship and due to differences in the chosen values of the permeability and the relative permeability saturation function. The latter two values are important for the water uptake

rate by the bentonite and depth of penetration for the wetting front, thus influence the modelled RH as well.

The measured and modelled water uptake is compared in Fig. 15. During the hydration phase about 270 g of water infiltrated into the column. The modelling results of several teams show water uptake values that are very close to the measurements, but the lower bound of the estimations goes down to about 160 g before the end of test. The water balance during the hydration phase is reflected in the modelling results of the RH. Results of teams with a lower water uptake over time show typically lower values for the RH at Sensor 1. The prediction of the water saturation for 20,000 h (15,000 h after start of hydration) is shown in Fig. 12c. The teams predict a penetration of the water infiltration front between 25 and 35 cm over the 15,000 h of the hydration phase of the experiment. A validation of the water saturation profile is not yet possible because the column has not been dismantled. Measured cumulative water uptake became proportional to t0.47t0.47 within hours (Fig. 15), consistent with the t1/2t1/2 cumulative inflow behaviour expected for one-dimensional diffusion into a porous medium. The models reached this characteristic behaviour at late times, differing somewhat on the details of early-time inflow and rate of inflow. The different early-time behaviour is probably due to differences in gridding and representation of the boundary condition, which are important while the front is confined to a few grid cells. The late-time inflow rate is controlled by the unsaturated permeability distribution over the wetting front.

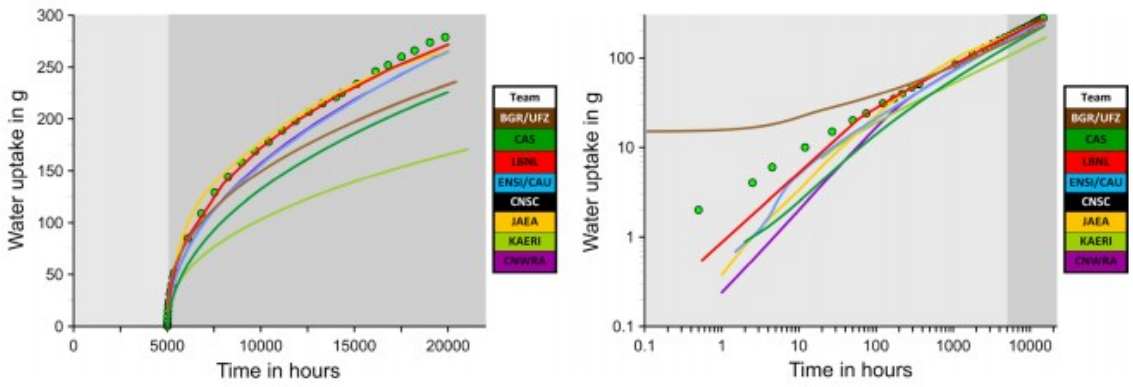

Fig. 15 Measured (dots) and modelled (lines) water uptake of the column during the heating (light grey area) and the hydration phases (dark grey area) with linear scale (left) and log–log scale (right)

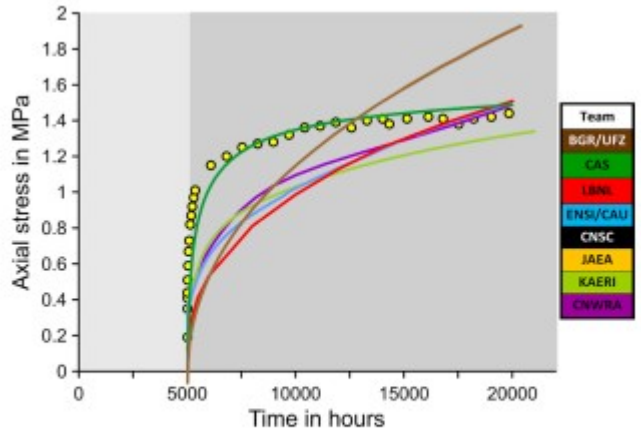

Fig. 16 Measured and modelled axial stress due to swelling during the heating (light grey area) and the hydration phases (dark grey area)

The water uptake during the hydration phase causes swelling of the bentonite, and the resulted axial stress is measured at the top of the column. Several teams considered an elastic deformation where the maximum swelling pressure is related to the water saturation. The comparison in Fig. 16 of the modelling results with the measurements indicates that a maximum swelling pressure of 4 MPa (Table 3) might be reasonable for describing the bentonite behaviour. Paralleling the water inflow, the models reached this characteristic behaviour at late times, differing somewhat on the details of early-time axial stress. As with the water inflow, the different early-time axial stress behaviour is probably due to differences in gridding and representation of the boundary condition, which are important while the front is confined to a few grid cells. The late-time inflow rate, and consequentially the axial stress, is controlled by the unsaturated permeability distribution over the wetting front.

The teams used a variety of constitutive relationships to calculate the change in stress due to swelling, usually based on the change in saturation or change in capillary pressure. Illustrated in Fig. 16, the CAS model best matches the general measured characteristic of a rapid response in axial pressure at early times with relatively insensitive responses at later times, although the model somewhat underestimates the cumulative water uptake. The CAS relative permeability model promotes rapid penetration of water at relatively low saturations, matching the measured relative humidity at the two lower sensors reasonably well during the hydration period while substantially underestimating the relative humidity at the upper sensor.

Based on the behaviour and parameterization of the CAS model compared with the other models and the physical behaviour during the column test, the water permeability and retention relationships may be more consistent with the CAS model at low saturations and more consistent with the other models at high saturations. One explanation would be that (1) the CAS model better represents the macropore system prior to swelling, (2) the other models

better represent the clay system after swelling and (3) the system switches between them. The permeability decreases with increasing saturation for the granular bentonite, at least in the middle range of saturation, as might be expected when permeable macropores shrink as the granular bentonite swells.

Summary and conclusions

The coupled THM processes will be an important aspect influencing the near-field evolution of a deep geological repository in argillaceous host rocks. The understanding of the involved processes, the knowledge about the relevant parameters and the capability for predictive modelling are key elements for determining a plausible range of scenarios for that evolution. The column experiment with MX-80 bentonite carried out at CIEMAT helped to improve the understanding of the behaviour of the bentonite, which might be a component of the multi-barrier system. With the selection of this experiment as one step within the Task B1 of DECOVALEX-2015 it was possible to derive a suitable set of parameters describing the THM behaviour of bentonite as a preparatory step for the modelling of the HE-E experiment.

The column experiment consists of two phases, a heating phase followed by a heating and hydration phase. During the heating phase, the initial water saturation is redistributed within the column whereas the resaturation of the pores due to water infiltration can be observed in the heating and hydration phase. The measured temperature and relative humidity can be used to derive a parameter set to describe the observed behaviour of bentonite. Important parameters are the heat conductivity and its dependence on water saturation, the water retention function, the permeability and the relative permeability and its dependence on the degree of saturation.

Eight modelling teams developed their own THM-coupled models, using six different codes. Six teams used a 2D axisymmetric approach and two teams developed a 3D model. In order to consider the heater in the model, some of the teams applied the temperature as boundary condition, partly combined with a lateral heat loss coefficient, while three teams used the heat power as a source term and applied the laboratory temperature as the boundary condition. The comparison of the modelled temperature at the heater shows a good agreement with the measurements.

Each of the teams calibrated the THM parameters for the granulated bentonite mixture. The eight parameter sets are fairly similar and allow a satisfactory reproduction of the THM measurements by all models. The modelling results for the temperature evolution over time are in good agreement between the teams and with the measured data. In particular, the changes of the temperature due to the modification of the insulation and the adaption of the heat power during the course of the experiment are reproduced quite well. This underlines that the thermal system of the experiment seems to be well understood.

Reproducing the relative humidity was much more challenging because more parameters are needed to describe the hydraulic behaviour of bentonite. Capturing the relative humidity dynamics requires that a model adequately addresses (1) temperatures; (2) temperature-dependent relationships between saturation, capillary pressure, vapour pressure and relative humidity; (3) saturation-dependent liquid redistribution; and (4) supply of water from the water source through the hydration system and porous stone to the top of the column. The modelling results of the teams reproduce in general all changes of the relative humidity over time at the different sensors, both for vapour-dominated diffusion during the heating phase and combined liquid and vapour transport during the heating and hydration phase. Some of the models show a very good agreement with the measurements. The spread of the modelling results increases with time, reaching total values of 20% and more. The increasing spread with time may be because the end points of the relationship between capillary pressure and water saturation relationship are less well defined. Additional experimental investigations may help to limit the range of possible capillary pressure–water saturation relationships. The parameter sets were also robust enough to predict the water penetration during the infiltration phase of the experiment. The teams predict a penetration of the water infiltration front between 25 and 35 cm over the 15,000 h of the hydration phase of the experiment. A validation of the water saturation profile is not yet possible because the column has not been dismantled.

The teams found that heat loss was significant during analysis of the temperature measurements and the determination of the thermal parameters. Only a fraction of the heat power resulted in heat entering the bentonite caused by the low heat conductivity of the bentonite and highly conductive steel components. It was possible to quantify the amount of heat leaving the experimental set-up below the bentonite-filled column using literature data constraining the possible thermal parameters and explicitly modelling the entire system. This shows, that a throughout analysis of heat flow and the heat balance is supported by simulation of the complete laboratory set-up, including all shells and insulation effects.

The hydraulic parameters determined during the heating phase at uniform initial water content not only showed the ability of each team’s model to reproduce the system evolution during this phase but also proved robust enough to predict the measurements of the infiltration tests. Although slight different approaches were used by the teams, generally modelling results are very close to the measurements. This emphasizes an improved understanding of ongoing THM processes investigated in this laboratory test. These parameters are also consistent with data from the literature.

The teams were all generally successful in representing the general dynamics of the water balance as measured by the relative humidity sensors and water uptake, although the models disagreed on the magnitude and timing of the responses. All of the models produced relative humidity

responses after a step change in temperature that were generally similar to the measurements. During the hydration period, all of the models showed a relatively large increase in relative humidity at Sensor 1, plateauing below full saturation, and a delayed increase at Sensor 2 that was still increasing at the end of the experiment. During the hydration period, each team's results generally agreed more closely in saturation below the wetting front (Sensors 2 and 3) and more closely in relative humidity in the wetted zone (Sensor 1). The water uptake during the hydration phase causes the swelling of the bentonite and the resulting axial stress is measured at the top of the column. Several teams considered an elastic deformation where the maximum swelling pressure is related to the water saturation although the measurements provided did not allow for an in-depth analysis of the mechanical components of the models.

This paper thus shows that joint model comparison is valuable in that they provide insights into the uncertainty of these predictions, as indicated by the spread of the model results, and also enhance process understanding and parameterization capabilities. This is a necessary step for the prognosis of long-term effects induced by nuclear waste repositories.

Acknowledgements

The members of Task B1 express their thanks for the financial support provided by the Funding Organisations of the DECOVALEX-2015 project, and for measured data from experiments supplied by the EU-PEBS project. CAS team's work was financially supported by international cooperation project of Chinese Academy of Sciences (Nos. 115242KYSB20160017, 115242KYSB20160024). CAU was financially supported by ENSI. The statements made in the paper are, however, solely those of the authors and do not necessarily reflect those of Funding Organisation(s). Also, no responsibility is assumed by the authors for any damage to property or persons as a result of operation or use of this publication and/or the information contained. The views expressed herein do not necessarily reflect the views or regulatory positions of the U.S. Nuclear Regulatory Commission (USNRC), and do not constitute a final judgment or determination of the matters addressed or of the acceptability of any licensing action that may be under consideration at the USNRC.

References

Armand G (2015) Task proposal for the international DECOVALEX-2019 project, Nov. 2015, Wakkanai, Japan

Ballarini E, Graupner B, Bauer S (2017) Thermal–hydraulic–mechanical behavior of bentonite and sand-bentonite materials as seal for a nuclear waste repository: numerical simulation of column experiments. Appl Clay Sci 135:289–299. https://doi.org/10.1016/j.clay.2016.10.007

Garitte B, Nguyen S, Barnichon JD, Graupner B, Lee L, Maekawa K, Ofoegbu G, Manepally C, Dasgupta B, Fedors R, Pan P, Feng XT, Rutqvist J, Chen F,

Birkholzer J, Wang W, Kolditz O, Shao H (2016) Modelling the Mont-Terri HE-D experiment for the thermal–hydraulic–mechanical response of a bedded argillaceous formation to heating. Submitted to Environmental Earth Sciences

Garitte B, Shao H, Wang XR, Nguyen TS, Li Z, Rutqvist J, Birkholzer J, Wang WQ, Kolditz O, Pan PZ, Feng XT, Lee C, Graupner BJ, Maekawa K, Manepally C, Dasgupta B, Stothoff S, Ofoegbu G, Fedors R, Barnichon JD (2017) Evaluation of the predictive capability of coupled thermo-hydro-mechanical models for a heated bentonite/clay system (HE-E) in the Mont Terri Rock Laboratory. Environ Earth Sci 76:64. https://doi.org/10.1007/s12665-016-6367-x

Gaus I, Wieczorek K, Schuster K, Garitte B, Senger R, Vasconcelos R, Mayor JC (2014a) EBS behaviour immediately after repository closure in a clay host rock: HE-E experiment (Mont Terri URL). Geol Soc Spec Publ. https://doi.org/10.1144/SP400.11

Gaus I, Garitte B, Senger R, Gens A, Vasconcelos R, Garcia-Sineriz JL, Trick T, Wieczorek K, Czaikowski O, Schuster K, Mayor JC, Velasco M, Kuhlmann U, Villar MV (2014b). The HE-E Experiment: lay-out, interpretation and THM modelling. Nagra Arbeitsbericht NAB pp 14–53

Hoffmann C, Alonso EE, Romero E (2007) Hydro-mechanical behaviour of bentonite pellet mixtures. Phys Chem Earth 32:832–849

Itasca (2012) FLAC3D (fast Lagrangian analysis of continua in 3 dimensions), Version 5.0. Itasca Consulting Group, Minneapolis

Itasca Consulting Group (2011) FLAC V 7.0, fast Lagrangian analysis of continua, user’s guide. Itasca Consulting Group, Minneapolis

Klinkenberg LJ (1941) The permeability of porous media to liquids and gases. In: Drilling and production practice, American Petroleum Institute, pp 200–213

Kolditz O, Bauer S (2004) A process-oriented approach to computing multi-field problems in porous media. J Hydroinformatics 6:225–244

Kolditz O, Bauer S, Bilke L, Böttcher N, Delfs JO, Fischer T, Görke UJ, Kalbacher T, Kosakowski G, McDermott CI, Park CH, Radu F, Rink K, Shao H, Shao HB, Sun F, Sun YY, Singh AK, Taron J, Walther M, Wang W, Watanabe N, Wu Y, Xie M, Xu W, Zehner B (2012) OpenGeoSys: an open-source initiative for numerical simulation of thermo-hydro-mechanical/chemical (THM/C) processes in porous media. Environ Earth Sci 67(2):589–599. https://doi.org/10.1007/s12665-012-1546-x

McWhorter DB, Sunada DK (1990) Exact integral solutions for two-phase flow. Water Resour Res 26(3):399–413

Müller HR, Weber HP, Koehler S, Vogt T (2012) The full-scale emplacement (FE) experiment at the Mont Terri Rock Laboratory. Clays in natural and

engineered barriers for radioactive waste confinement. In: 5th International meeting, book of abstracts (p. 923). France

Nguyen S, Li Z, Garitte B, Barnichon JD (2016) Modelling a heater experiment for radioactive waste disposal. ICE Environmental Geotechnics. In press

Ohnishi Y, Shibata H, Kobayashi A (1985) Development of finite element code for the analysis of coupled thermo-hydro-mechanical behaviors of a saturated–unsaturated medium. In: Proc. of int. symp. on coupled process affecting the performance of a nuclear waste repository, Berkeley, pp 263–268

Pan PZ, Feng XT (2013) Numerical study on coupled thermo-mechanical processes in Äspö Pillar stability experiment. J Rock Mech Geotech Eng 5(2):136–144

Pan PZ, Feng XT, Hudson JA (2009a) Study of failure and scale effects in rocks under uniaxial compression using 3D cellular automata. Int J Rock Mech Min Sci 46(4):674–685

Pan PZ, Feng XT, Huang XH, Cui Q, Zhou H (2009b) Coupled THM processes in EDZ of crystalline rocks using an elasto–plastic cellular automaton. Environ Geol 57(6):1299–1311

Pearson FJ, Arcos D, Bath A, Boisson JY, Fernández AM, Gäbler HE, Gaucher E, Gautschi A, Griffault L, Hernán P, Waber HN (2003). Geochemistry of water in the Opalinus clay formation at the Mont Terri Laboratory, Mont Terri Project, TN 2003-03, SWISSTOPO

Rizzi M, Seiphoori A, Ferrari A, Ceresetti D, Laloui L (2012) Analysis of the behaviour of the granular MX-80 bentonite in THM-processes. Aktennotiz AN 12-102

Rutqvist J, Wu Y-S, Tsang C-F, Bodvarsson G (2002) A modeling approach for analysis of coupled multiphase fluid flow, heat transfer, and deformation in fractured porous rock. Int J Rock Mech Min Sci 39:429–442

Rutqvist J, Zheng L, Chen F, Liu H-H, Birkholzer J (2014) Modeling of coupled thermo-hydro-mechanical processes with links to geochemistry associated with bentonite-backfilled repository tunnels in clay formations. Rock Mech Rock Eng 47:167–186

Seiphoori A (2015) Thermo-hydro-mechanical characterisation and modelling of Wyoming granular bentonite. Nagra technical report 15-05

Stothoff S, Painter S (2016) xFlo version 1.1 user’s manual DECOVALEX-2015 version; NRC ADAMS accession no. ML16167A315. San Antonio, Texas: Center for Nuclear Waste Regulatory Analyses

Stothoff S, Manepally C, Ofoegbu G, Dasgupta B, Fedors R (2015) Modeling thermohydrological-mechanical behavior of granular bentonite in a laboratory column test. NRC ADAMS accession no. ML15324A128. San Antonio, Texas: Center for Nuclear Waste Regulatory Analyses

Tang AM, Cui YJ (2006) Determining the thermal conductivity of compacted MX80 clay, unsaturated soils 2006. Reston, Virginia

Tang AM, Cui YJ (2010) Effects of mineralogy on thermo-hydro-mechanical parameters of MX80 bentonite. J Rock Mech Geotech Eng 2(1):91–96

Villar MV (2005) MX-80 bentonite. Thermo-hydro-mechanical characterization performed at CIEMAT in the context of the prototype project. Informes Técnicos Ciemat 1053 Febrero, 2005. Departamento de Impacto Ambiental de la Energía

Villar MV (2013) PEBS project: long term THM tests reports: isothermal infiltration tests with materials from the HE-E (deliverable no: D2.2-7.2)

Villar MV, Martín PL, Gómez-Espina R, Romero FJ, Barcala JM (2012) THM cells for the HE-E test: setup and first results. PEBS report D2.2.7a. CIEMAT technical report CIEMAT/DMA/2G210/02/2012. Madrid, p 34

Villar MV, Martín PL, Romero FJ (2014) Long-term THM tests reports: THM cells for the HE-E test: update of results until February 2014. Deliverable-no: D2.2-7.3. CIEMAT technical report IEMAT/DMA/2G210/03/2014

Wang Q, Tang AM, Cui YJ, Delage P, Gatmiri B (2012) Experimental study on the swelling behaviour of bentonite/claystone mixture. Eng Geol 124(2012):59–66. https://doi.org/10.1016/j.engeo.2011.10.003

Wang X, Shao H, Wang W, Hesser J, Kolditz O (2015) Numerical modelling of heating and hydration experiments on bentonite pellets. Eng Geol 198:94–106

Wieczorek K, Miehe R, Garitte B (2011). Measurement of thermal parameters of the HE-E buffer materials. Deliverable (D-No: 2.2-5) PEBS (contract number: FP7 249681)

Wieczorek K, Miehe R, Garitte B (2013) Thermal characterisation of HE-E buffer. Deliverable (D-No: 2.2-9) PEBS (contract number: FP7 249681)

Wileveau Y (2005) THM behaviour of host rock (HE-D experiment): progress report September 2003–October 2004. Mont Terri technical report TR2005-03

Wileveau Y, Su K (2007) In situ thermal experiment carried out in Opalinus clay and Callovo-Oxfordian claystones by Andra—experiment set-up and measurement results. ANDRA report, Paris, p 2007